Journal of Applied Meteorology and Climatology

The DOI for this manuscript is doi: 10.1175/JAMC-D-13-063.1

Muñoz, R., M. Falvey, M. Araya, and M. Jacques-Coper, 2013: Strong down-valley low-level jets over the Atacama Desert: observational characterization. J. Appl. Meteor. Climatol. doi:10.1175/JAMC-D-13-063.1, in press.

Strong down-valley low-level jets over the Atacama Desert: observational characterization

Ricardo C. Muñoz, * Mark J. Falvey

Dept. Geophysics, University of Chile, Santiago, Chile

Marcelo Araya

Centro Nacional del Medio Ambiente, Santiago, Chile

Martin Jacques-Coper

Oeschger Centre for Climate Change Research and Institute of Geography, University of Bern, Bern, Switzerland

* *Corresponding author address:* Ricardo C. Muñoz, Dept. Geophysics, University of Chile, Av. Blanco Encalada 2002, Santiago, Chile.

E-mail: rmunoz@dgf.uchile.cl

ABSTRACT

The near-surface wind and temperature regime at three points in the Atacama Desert of northern Chile is described using two-year multi-level measurements from 80-m towers located in an altitude range between 2100 and 2700 m ASL. The data reveal the frequent development of strong nocturnal drainage flows at all sites. Down-valley nose-shaped wind speed profiles are observed with maximum values occurring at heights between 20 m and 60 m AGL. The flow intensity shows considerable inter-daily variability and a seasonal modulation of maximum speeds, which in the cold season can attain hourly average values larger than 20 m s^{-1}. Turbulent mixing appears significant over the full tower layer, affecting the curvature of the nighttime temperature profile and possibly explaining the observed increase of surface temperatures in the down-valley direction. Nocturnal valley winds and temperatures are weakly controlled by upper-air conditions observed at the nearest aerological station. Estimates of terms in the momentum budget for the development and the quasi-stationary phases of the down-valley flows suggest that the pressure gradient force due to the near-surface cooling along the sloping valley axes plays an important role in these drainage flows. A scale for the jet nose height of equilibrium turbulent down-slope jets is proposed, based on surface friction velocity and surface inversion intensity. At one of the sites this scale explains about 70% of the case-to-case observed variance of jet nose heights. Further modeling and observational work is needed, however, in order to better define the dynamics, extent and turbulence structure of this flow system, which has significant wind-energy, climatic and environmental implications.

1. Introduction

The Atacama Desert in northern Chile is renowned for its hyper-aridity caused by geographic and climatic factors (Garreaud and Aceituno 2007; Garreaud et al. 2010; Garreaud 2010). To its east, the Andes Cordillera rises to altitudes that exceed 6000 m precluding moisture transport from the Amazon basin. To its west, the subtropical South East Pacific (SEP) Anticyclone and the cold coastal waters of the Chile-Peru current provide for a very stable large-scale environment. The climate of the Atacama Desert is thus characterized by low synoptic variability, very infrequent precipitation, extremely clear skies (except near the coast where stratocumulus are common), intense solar radiation, large diurnal thermal amplitudes, strongly sloping topography, and a very arid surface with little vegetation and negligible moisture availability. In terms of surface winds, these characteristics constitute almost ideal conditions for the observation of terrain-induced thermal circulations. The existence in the Atacama Desert region of near-surface winds driven by the thermal contrasts of the cold ocean, the desert and the Andes has been described by Schmidt (1999) and documented through short-term field campaigns by Rutllant and Ulriksen (1979) and Rutllant et al. (2003). These winds have been hypothesized to affect the lower-tropospheric stability and regional hyper-aridity (Rutllant et al. 2003) and the transport of continental aerosols (natural and anthropogenic) towards the SEP stratocumulus layer over the ocean to the west (Chand et al. 2010). However, comprehensive and extended datasets describing surface winds in the Atacama Desert have only recently become available. Over the last few years Chilean energy authorities have conducted a series of projects aimed at evaluating the wind energy potential of the northern part of the country. As part of these efforts, three 80-m meteorological towers with multi-level wind and temperature measurements were installed in the Atacama Desert between 22 ^{o}S and 23 ^{o}S. The main purpose of the present communication is to document the strong nocturnal down-valley flows unveiled by these observations. In particular, our objectives are 1) to describe the mean characteristics and variability of the down-valley flow, with special emphasis on the local co-variability of wind and temperature

profiles at each site, and 2) to provide an observational evaluation of the regional and local controls affecting these flows. The wind energy implications of these measurements, as well as their numerical modeling and predictability assessment are being addressed in parallel studies and will be reported elsewhere.

The variability of near-surface winds is affected by factors spanning a large range of scales. At the synoptic-scale, pressure gradients provide for the day-to-day variability of surface winds, while local obstacles and surface properties determine their finer-grade structure. In between, regional topography can be a powerful forcing of surface winds, playing a prominent role in shaping their diurnal cycles in connection to mesoscale pressure gradients ensuing from the daytime/nighttime heating/cooling of complex terrain. Whiteman (2000) reviews the basic forms in which this thermal forcing manifests, distinguishing between slope winds, along-valley winds, cross-valley winds, and mountain-plain winds, depending on the temperature contrasts driving the pressure gradients (along a slope, within a valley or between a valley and a plain, across the valley sides, or between a mountain and a plain, for each of the aforementioned cases, respectively). Here we describe the slope-wind and along-valley wind mechanisms, which appear to be most relevant to the flows presented in this work.

Nocturnal slope winds (also referred to as katabatic winds) are driven by an along-the-slope pressure gradient arising as the air close to an inclined surface cools relative to the air above. Their study has a long history, with various authors considering different additional terms in the momentum budget to compensate the buoyant downward acceleration. A comprehensive dynamical analysis of this mechanism has been given by Mahrt (1982). In typical conditions, katabatic winds are generally weak and shallow and are considered relevant to explain nocturnal flow down the slope of valley sides. Strong and extensive katabatic flows, however, have been reported over Antarctica (Parish 1982; Parish and Bromwich 1987), where the long polar night, the cold ice-covered surface and the topography combine to produce regions over which "extraordinary" katabatic winds develop (Bromwich 1989;

Wendler et al. 1997). They are characterized by near-surface average speeds between 10 and 30 m s^{-1} and very high directional persistence. Nocturnal down-slope and down-valley katabatic flows have also been studied in the Rocky Mountains in western North America (e.g. Savage et al. 2008; Whiteman and Zhong 2008). Maximum wind speeds in these cases are generally less than 10 m s^{-1}, with drainage layers that can reach up to ∼250 m AGL.

The nocturnal down-valley wind mechanism, on the other hand, does not require an inclined bottom surface at all, as illustrated by the horizontal valley floors used in idealized modeling studies of these flows (e.g. Schmidli et al. 2011). The along-valley pressure gradient driving the surface winds in this case is caused by the relative cooling of the valley's atmosphere as compared to a nearby plain (Whiteman (1990); 2000). Crucial in this mechanism is the geometric shape of the valley in the cross-valley and along-valley directions, as well as the surface energy budget and radiative effects. Besides their thermal forcing, valley winds can also be affected by large-scale winds and pressure gradients. Whiteman and Doran (1993) categorize these influences in terms of the relationship between the directions of the valley winds and the upper-air (geostrophic) winds, defining the mechanisms of downward momentum transport (with valley winds following closely the upper-air wind direction), forced channeling (with valley winds aligned to the valley axis in the direction of the upper-air wind) and pressure driven channeling (with valley winds aligned to the valley axis in the direction of the upper-air pressure gradient, perpendicular to the upper-air geostrophic wind).

Although the mechanisms described above appear well defined and distinct, real cases in complex terrain will generally be affected by a combination of them. In our case, for example, although the three sites studied are located along valley axes, we cannot discard a priori effects of mountain-plain winds associated to the large Andes Cordillera massif existing to the east, nor slope-wind effects due to the inclination of the valley floors. Therefore, following Whiteman (1990), perhaps a proper name for the nocturnal flows documented here would be the mixed term of drainage winds. We will use the term down-valley winds, however,

considering that this is their most persistent direction, leaving the issue of the dynamical forcing to a discussion in the final part of this paper, and to subsequent modeling work.

2. Site and data

a. Regional topography

Figure 1 shows the topography of the study region and the location of the three 80-m towers analyzed here. All are located along the central axes of wide, gently sloping valleys. Tower SGE is located along Arriero Creek, an east-west oriented dry streambed close to the town of Sierra Gorda. Towers CAN and CAO are located along the Loa River valley, up-valley and down-valley of Calama City ($\sim$ 140,000 inhab.), respectively. At the CAO site the valley is also east-west, while at CAN the valley is oriented north to south. Figure 2 shows a closer look at the terrain surrounding the towers, including along- and cross-valley topographical profiles. The average slopes along the valley axes are relatively steep, with values ranging between 1.3 and 1.7%, while the cross-sections show some differences between the three sites. CAN, for example, is located where the Loa River valley widens significantly as compared with the up- and down-valley topography, resulting in a local cross-valley transect with a $\sim$30 km flat floor. In contrast, transects at CAO and SGE show a well defined U-shape, deeper and wider at CAO as compared to SGE. These variations in relief may explain some of the differences that the down-valley winds exhibit in each site, as shown in Section 3.

b. Available data

The three towers were installed in February 2011. Figure 3 provides an overview of hourly wind speeds at 40 m available at the time of this writing. As the planned measuring period of the towers was limited to 2 years and our focus of analysis will be the cold season

between May-October, the datasets can be considered complete for our purposes. Figure 3 shows several gaps in data availability at CAN and CAO. Those in 2011 were mostly due to signal interference of the remote data transmission, which was corrected in August 2011, while the lost month of June 2012 at CAO was due to vandalism. For the months from May to October, data availability at CAN, CAO and SGE amounts to 86%, 81%, and 99%, respectively, providing a fair to good representation of winter-spring conditions of years 2011-2012, which presented weak-moderate La Niña conditions, as indicated by the Multivariate ENSO Index of Wolter and Timlin (2011).

The main measurements in the towers are wind speed at 5 levels, wind direction at 3 levels, and air temperature at 3 levels (heights and sensors provided in Table 1). Each of the sensors used included individual calibration certificates against reference standards, making their observations directly comparable among them. Ancillary meteorological data include near-surface relative humidity, atmospheric pressure, and solar radiation, all data available as 10-minute averages computed from 1 Hz samples. As a means of relating the tower measurements to upper-air conditions, we use 12 UTC (08 LT) vertical profiles of wind and temperature measured at the operational radiosonde station of Antofagasta, located at the coast about 150 km to the WSW of SGE (see Fig. 1). A long-term characterization of the regional lower troposphere based on these upper-air observations can be found in Muñoz et al. (2011).

c. Down-valley flow indices

The observational characterization presented in Section 3 is based upon indices describing the intensity, directional persistence, jet nose height, and stability of the nocturnal flows observed at the three sites. These indices are defined and justified next.

At the three sites considered the daytime and nighttime low-level wind regimes are strongly differentiated, as shown by the mean diurnal cycles of 40-m wind speed shown in Fig. 4a. The nighttime phase of the wind regime begins a few hours after sunset, at

around 21 LT, when wind speeds start intensifying, attaining maximum mean values by sunrise, at about 07 LT. The daytime phase, on the other hand, has maximum speeds between 15 and 18 LT. Wind directions also show strong contrasts between day and night regimes, as illustrated by the most frequent directions represented with circles in Fig. 4a. At CAN, nighttime (daytime) flow is predominantly from the NNE (SW), while at CAO and SGE the corresponding directions are from the ENE (W). Based on the well-defined and regular diurnal pattern of near-surface winds, the 02-06 LT period is chosen as representative of well-developed nighttime flows.

Figures 4b-d show the joint wind speed-wind direction frequency distribution at 40 m AGL for all observations in the 02-06 LT period. The very marked directional preference of the nighttime flow is evident in these figures with 81%, 92%, and 94% of the observations at these hours falling in a 45^o sector centered at 10^o, 75^o, and 80^o for stations CAN, CAO, and SGE, respectively. We shall call these sectors as down-valley direction sectors, and define, for each night and site, the index FDV40 as the fraction of 40-m wind direction observations in the 02-06 LT period falling in the corresponding down-valley direction sector. Values of FDV40 are generally high, indicative of the large topographic control of these nocturnal flows. The wind intensity, however, is more variable, as shown by the wind speed ranges in Figs. 4b-d), with 10-minute averages varying generally between 5 m s^{-1} and 20 m s^{-1}. The simple average of 40-m wind speed in the 02-06 LT (WS40) period will be used in Section 3a as intensity index for the nocturnal flows at each site (their variability has been shown in Fig. 3). In Sections 3b and 3c, on the other hand, the 40-m down-valley projected wind speed (DVWS40) will be used as an index better suited for comparing down-valley flow intensities among the different sites.

The availability of wind speed measurements in the 10-80 m height range has allowed the observation that nighttime flows at these sites frequently take the form of a low-level jet, with wind speeds reaching a local maximum at a certain height above the surface. To describe this, we define the ZX index as the height of the wind speed maximum for each

10-minute observation. Figure 5 shows the frequency distribution of ZX and how it varies in the 18-08 LT period. While during daytime and at the beginning of the evening transition ZX corresponds almost always to the highest measurement level, with no indication of a low-level jet, during the night the most common values of ZX are between 20 m and 60 m AGL depending on site and hour. In the early evening the maximum wind speeds are most commonly found in the first measurement level (10 m) at all three stations. As time passes, the nose of the jet profile increases in height, being typically at 20 m at SGE and at 40 m at CAN and CAO, suggesting that the evening wind reversal is a bottom-up process. The nighttime ZX frequency distributions are less variable at SGE, with more variability observed at the other two sites. At CAO, in particular, a secondary maximum is observed after 02 LT at the 80-m level, indicating that in many cases the nose of the jet is further aloft, or there is no jet structure at all.

Finally, the static stability in the tower layer will be described by means of indices computed as 02-06 LT averages of the difference of temperatures measured at the upper (DTU=T80-T40) and the lower (DTL=T40-T02) levels equipped with temperature sensors. An additional temperature-related index will be the 02-06 LT average of the curvature of the temperature vertical profile, estimated as CT=T80-2*T40+T02.

3. Results

a. Characterization of down-valley jets and stability

For each site we define a down-valley low-level jet (DVJ) case as a night in which the following conditions are met:

- FDV40 $>$ 85%, i.e. more than 85% of the 02-06 LT wind direction observations fall in the down-valley direction sector, and
- ZX $<$ 80 m in more than 85% of the 02-06 LT observations.

These conditions are rather strict in demanding persistent down-valley nose-shaped wind profiles, but they still permit the inclusion of a significant number of cases, as illustrated by the time series in Fig. 3 and the occurrence frequency of DVJ cases in Fig. 6a. Site SGE has the maximum percentage of cases along the year (79% annual average), while CAN and CAO have bi-monthly frequencies between 20% and 60%. It must be stressed that cases left out may also be low-level jets, but they have a larger directional variability or have maximum speeds at 80 m or above (especially at CAO), rendering them less suited for characterizing wind and temperature profiles below and above the jet nose.

Figure 6b describes the variability of DVJ intensities, as measured by the inter-quartile ranges of WS40 for each site. Typical magnitudes vary in the 5-18 m s^{-1} range, with an appreciable seasonal modulation showing larger values between May and October (austral winter and spring). Figures 6c-d describe, for DVJ cases, the variability of the stability indices DTL and DTU, respectively. The stability closer to the surface shows little seasonal variation, with temperature differences typically in the 2-4 ^{o}C range all year long. The stability in the upper layer, however, has a strong seasonal modulation in phase with the jet intensity (Fig. 6b). This co-variability between wind speed and temperature profiles in DVJs is further analyzed next.

In order to, at least partially, filter out the seasonal co-variability of winds and stability, we restrict the subsequent analysis to the months from May to October, leaving 169, 118 and 300 DVJ cases for CAN, CAO, and SGE, respectively. Figure 7 displays the mean vertical profiles of wind speed and temperature, distinguishing between cases of weak and strong DVJs (using the median of WS40 as discriminator). A connection between the wind speed and temperature profiles is suggested by Fig. 7, although not as much in terms of the bulk temperature gradient or stability, but rather in terms of the curvature of the temperature profile. Indeed, especially at CAN and SGE, the curvature of the mean temperature profiles changes sign between the weak and strong DVJs. The case-to-case co-variability between temperature and wind speed profiles is examined in Fig. 8. At the three sites there is a

marked contrast in the relationship between the DVJ intensity and the stability in the lower and the upper layers. While stronger down-valley flows are generally associated to reduced stability in the lower layer, the opposite association exists with the stability in the upper layer. As a result, a positive correlation between the intensity of the flow and the bulk curvature of the temperature profile is observed, as shown in the rightmost scatter plots of Fig. 8. These relationships are clearer at CAN and SGE in which CT becomes positive in a large number of cases. At CAO, however, only few cases reach a positive curvature in the temperature profile. Reasons for the differences among sites have not been elucidated yet, but topographic differences along and across the valleys may probably play a role (see Fig. 2).

We interpret the positive correlation between temperature curvature and wind speed as a consequence of the curvature-turbulence relationship proposed by André and Mahrt (1982) (see also Edwards et al. 2006). According to this mechanism, turbulent mixing in the stable boundary layer induces a positive curvature in the temperature profile, opposite to the effect of longwave radiation. As turbulence may be expected to increase with stronger low-level winds, this mixing effect might explain the right hand scatter plots in Fig. 8. Unfortunately, direct measurements of turbulence are not available at these towers. As surrogates, we present in Fig. 9 vertical profiles of turbulence-related variables. The upper panels show distributions of gradient Richardson numbers (Ri) computed based on the temperature and wind profiles. Three layers can be recognized in these figures. Below the jet nose all three sites show very low Ri values, indicative that in this layer wind shear production can sustain turbulence in the presence of buoyant consumption. Largest values of Ri are found in the region of the jet nose due to the low shear existing there. Above the jet, where shear is again significant, Ri values are smaller, but not as much as in the sub-jet layer (especially at CAO and SGE). Shear production in this layer may not be sufficient to sustain turbulence, although turbulence can still exist if transport from the sub-jet layer is important. As an approximation to the turbulence intensity in the different layers, the lower panels in Fig. 9

show vertical profiles of the standard deviation of wind speed (σ_{ws}) measured by the propeller anemometers, distinguishing again between weak and strong DVJ cases. Values of σ_{ws} in all levels are comparable, suggesting that turbulence exists throughout the layer sampled by the towers. Largest values of σ_{ws} are found in the lowest measurement levels, consistent with the smaller Ri values found there. The profiles also tend to present a minimum of σ_{ws} at the jet nose level, in accordance again with the small shear production there and the high Ri values. An interesting feature is the change of these mean profiles with DVJ intensity. The stronger down-valley flows are associated to larger values of σ_{ws} in the sub-jet layer, but to smaller values in the layer above the nose. The larger stability existing in this layer associated to the stronger DVJs (see center scatter plots in Fig. 8) may explain this relationship. The overall prevalence of turbulence over the full tower layer and its minimum at the level of the jet suggested by these observations are consistent with those reported by Conangla and Cuxart (2006) for a nocturnal jet of ~ 10 m s^{-1} intensity and ~ 65 m nose height measured with a 100 m instrumented tower in the north Castilian Plateau, Spain.

b. Regional control of down-valley flows and temperatures

1) Down-valley winds

We explore now the co-variability of winds between the three sites and with regional forcings. As flow intensity indices we consider the 40-m down-valley projected wind speed (DVWS40) averaged over hours 02-06 LT for the months of May to October. Upper panels in Fig. 10 show the scatter diagrams of DVWS40 measured at the three towers. A generally good relationship between the down-valley flow strength at all sites is appreciated, especially for the high-values range. The best correlation is found between stations CAO and SGE ($r \sim 0.91$), which may be explained by the fact that they are located in contiguous zonally oriented valleys, in contrast to the meridionally oriented valley of station CAN (see Fig. 2). Therefore, large-scale pressure patterns that modulate down-valley flows in the region may

produce a more similar control on CAO and SGE.

The Antofagasta radiosondes provide an opportunity for a first-order evaluation of the large-scale controls on the nocturnal down-valley flows. For this purpose, we computed the correlation coefficients between DVWS40 and three indices derived from the Antofagasta soundings (Table 2). In all cases the largest correlations are found for Antofagasta variables in the 2000-3000 m ASL range, coincident with the altitudinal range of the 80-m towers. The first row in Table 2 shows the correlation between the down-valley flows at the three sites and the winds measured by the 12-UTC soundings. More specifically, the correlation is with the component of the upper-air winds coming from the ESE-SE sector, for which the correlation was highest for the three sites. A modest zero-lag correlation, $r \sim 0.5$, is found, with no marked differences among sites.

The second and third rows in Table 2 quantify the relationship between the intensity of the down-valley winds and the free-troposphere temperature structure. The down-valley wind mechanism suggests that the relative cooling of the valley air mass relative to the free troposphere at the same altitude should enhance the drainage winds. Indeed, for the three sites the largest correlations found are those between DVWS40 and the difference between the Antofagasta temperature averaged in the 2000-3000 layer (TANTO) and the tower temperatures averaged over the three data levels (TZNIGHT). This suggests that the down-valley wind mechanism may be at work in these flows, especially considering that correlations with the temperature difference generally increase as compared to those calculated using the radiosonde temperature alone (comparing second and third row values in Table 2). Nonetheless, all these correlations are relatively modest, and the scatter plots associated to them display a large dispersion (not shown), which may be partially explained by the $\sim$ 200 km distance between Antofagasta and the tower sites.

2) Temperature patterns

Middle and lower panels in Fig. 10 show the scatter diagrams between DTL and DTU values among the three sites. The correlations in these cases are smaller than in the case of the flow strengths, suggesting that the adjustment of the temperature profile to the down-valley flow is influenced by local factors. In this regard, the small range of stabilities measured at CAO in comparison with CAN and SGE could be related to the presence of the city of Calama upwind of CAO. The large roughness associated to the urban land use may preclude the development of intense inversions near the surface.

In terms of the temperature comparison among the different sites, a noticeable feature apparent in Fig. 7 is the higher temperatures in CAO as compared to its up-valley counterpart CAN. While the down-valley mechanism requires colder temperatures upwind at the same altitude, near the surface the temperature usually drops in the down-valley direction, especially if the topography forces the drainage flow to accumulate and form cold pools. In our case, Figs. 7b-f show that the down-valley site CAO has a near-surface temperature about 2.5 ^{o}C higher than that measured at CAN. In order to better understand this regional temperature pattern, Fig. 11 shows the average nighttime temperatures measured at the three 80m-towers as a function of altitude. We have also included in the figure corresponding 5-m averaged temperatures of four additional 20-m towers existing in the same valleys (locations shown in Fig. 2). The general trend of warmer temperatures at lower sites is confirmed by all stations, provided the different heights above the ground of the measurements and the different valleys of each station are taken into account. The continuous vertical profile in Fig. 11 shows the corresponding temperature average of the 12 UTC (08 LT) operational radiosonde measurements available at the coast in Antofagasta (see Fig. 1). The well defined subsidence inversion very frequently observed at this location leaves a clear hallmark in the mean temperature profile, characterized by a conspicuous inversion in the 800-1500 m layer (Muñoz et al. 2011). The subsidence inversion, however, rarely exceeds 2000 m ASL leaving the altitude range occupied by the analyzed stations under the influence of the free tropo-

sphere above the inversion. Indeed, the mean lapse rate of the radiosonde profile is very close to that of the surface stations. Moreover, while the nighttime near-surface measurements are considerably colder than the radiosonde profile at the same altitude, the 80-m measurements are much closer, suggesting that the surface inversions in these valleys tend to match the free-tropospheric temperature (keeping in mind the differences in the times of the station temperatures and the upper-air temperatures in Fig. 11). These observations suggest that the turbulent mixing associated to the strong down-valley flows is capable of keeping the near-surface temperatures in the valleys coupled to the free-tropospheric thermal profile.

c. Slope-cooling forcing of down-valley flows

In the previous sub-section we assessed the down-valley wind mechanism as a factor of the observed nocturnal flows, by relating them to the regional wind and thermal structure. While some support for the down-valley mechanism was found, this observational work would not be complete without an estimate of the slope-wind mechanism as well. As pointed out in the Introduction, real complex-terrain winds are prone to be affected by various factors in different degrees, and considering the significant slope of these valley axes ($\sim 1.5\%$, see Section 2), the cooling of the sloping surface air might play a role as well.

Figures 12a-b show the mean evolution of the down-valley component of the wind and the near surface stability at the three sites. The existence of two distinct phases during nighttime is suggested by these plots. A transition phase occurs between 18 LT and 02 LT, in which the down-valley flow intensity increases steadily (Fig. 12a). Afterwards, between 02 and 07 LT, a quasi-stationary regime of flow and stability is observed. The 40m-02m stability evolution during the transition phase shows an interesting behavior (Fig. 12b). It changes sign at sunset (18 LT), just before the time when the down-valley flows begin to increase, then it reaches a maximum in the middle of the transition and it finally adjusts to a lower value in the quasi-stationary phase. Although the details of the transitions are different in each station, the initial and final states and the shape of the transition are similar for the

three of them. The joint evolution of down-valley flow and stability during the transition suggests a mutual adjustment. Development of the surface inversion appears to accelerate the flow in the down-valley direction, with the flow at some time becoming so intense that its accompanying turbulent mixing reduces the near-surface stability, and a sort of equilibrium between stability and flow strength is finally established.

Some quantification of the slope mechanism is possible based on the available observations. To do so, we compute the down-valley pressure gradient driven by a surface temperature inversion over a sloped surface. Let us model the temperature inversion as

$$T(z) = T_\infty - \Delta_o \exp(-z/H), \tag{1}$$

where T_∞ is the upper-air temperature, Δ_o represents the intensity of the surface cooling, H is the height scale of the inversion, and z is the local vertical coordinate. The hydrostatic equation applied to this temperature structure results in

$$\frac{dp}{dz} = -\frac{gp}{RT_\infty}\left(1 - \frac{\Delta_o}{T_\infty}\exp\left(-z/H\right)\right)^{-1}, \tag{2}$$

where g is the acceleration of gravity and R is the ideal gas constant for air. The three parameters T_∞, Δ_o, and H are assumed uniform in space, so that horizontal pressure gradients arise solely due to the along-slope change of altitude, Z, for a constant value of z, as given by $Z = Z_T(x) + z$, where Z_T is the surface altitude and x is the distance coordinate in the up-valley direction. Assuming a small slope, $s = dZ_T/dx$, and small perturbations with respect to density ρ_o, and temperature T_o, the horizontal pressure gradient at the surface in the up-valley direction is approximately

$$\frac{1}{\rho_o}\frac{\partial p}{\partial x} \sim sg\frac{\Delta_o}{T_o}. \tag{3}$$

If we estimate Δ_o based on the T40-T02 difference shown in Fig. 12b, then its linear time increase during the transition can be approximated by $\Delta_o \sim (5^o\mathrm{C}/4\mathrm{hr})t$, where t is time after sunset. Replacing this expression in (3) and integrating in time for a 4-hr transition, we obtain that the pressure gradient can support an increase of 18 m s^{-1} in the downslope

flow in the four hours (we have used $s \sim 0.015$, and $T_o \sim 300$ K). This value is quite large but of the same order as the ~ 12 m s^{-1} observed increase in downslope flow during the transition (Fig. 12a), the overestimation suggesting that turbulent friction plays a role as well. Indeed, the role of turbulence is presumably important after the stability and flow have mutually adjusted. If we assume that in the quasi-stationary regime a balance exists between the turbulence and pressure gradient forces, then

$$\frac{\partial \overline{u'w'}}{\partial z} \sim -sg\frac{\Delta_o}{T_o}, \tag{4}$$

where $\overline{u'w'}$ is the turbulent momentum flux. The left hand side of (4) can be estimated as

$$\frac{\partial \overline{u'w'}}{\partial z} \sim -\frac{u_*^2}{H_n}, \tag{5}$$

where u_* is the surface friction velocity and H_n is a height scale at which $\overline{u'w'} \sim 0$. Combining (4) and (5), an estimate for H_n is

$$H_n \sim u_*^2 \left(sg\frac{\Delta_o}{T_o} \right)^{-1}. \tag{6}$$

The friction velocity can in principle be related to the wind speed at 10 m AGL using atmospheric surface layer relationships. During the quasi-stationary regime, wind speed at 10 m AGL is ~ 10 m s^{-1} (Fig. 7) and assuming near-neutral conditions in the surface layer, we can estimate u_* by using a logarithmic wind profile and a surface roughness appropriate for a desert ($z_o \sim 10^{-3}$ m), obtaining $u_* \sim 0.4$ m s^{-1}. Figure 12b shows that in the equilibrium $\Delta_o \sim 5$ ^{o}C (we include also the temperature difference between 80 m and 40 m which in the equilibrium regime is significant), so that the scale height $H_n \sim 65$ m. This scale is higher but of the same order as the observed height of the jet nose (between 20 m and 60 m AGL according to Fig. 5), at which, by symmetry arguments, $\overline{u'w'}$ can indeed be argued to be close to zero, consistent also with the turbulence modeling of nocturnal jets by Conangla and Cuxart (2006) and Cuxart and Jiménez (2007). Two reasons can be thought of to explain the overestimation of H_n with respect to the observed nose jet heights: 1) the neutral assumption in the estimation of u_* produces probably an overestimation of u_*,

considering that near-surface conditions are more stable than neutral; 2) if the actual H_n is in the 20-40 m AGL range, then wind speed measurements at 10 m AGL fall probably outside the atmospheric surface layer (conventionally defined as the layer where turbulent fluxes change less than 10% from their surface values), so that the u_* estimate based on the 10 m wind speed is again questionable. Neither of these two considerations, however, invalidates the interpretation of (6) as an estimate for the nose height scale of an equilibrium turbulent down-slope jet. Application of (6) to explain the observed case-to-case variability of ZX produces the scatter plots in Figs. 12c-e. While the overestimation of nose height values persists, a positive correlation between H_n and ZX is found at the three sites, being largest at CAN, where about 70% of the observed ZX variance is explained by (6).

Summarizing this sub-section, we conclude that during the transient phase and during the quasi-equilibrium regime of these down-valley flows, the joint evolution of the stability and the flow intensity suggests that the down-slope pressure gradient due to the surface cooling and the turbulent wind stress are both important terms in their momentum budgets.

4. Summary and Conclusions

To the authors's knowledge, this communication provides the first extended ($\sim$2 years, 0-80 m AGL, 3 sites) documentation of the surface wind flow over the Atacama Desert region of Northern Chile. The most conspicuous feature of the observed wind regime is the existence of a strong nocturnal drainage flow with hourly averaged down-valley speeds reaching up to about 20 m s^{-1} during the cold season. The multi-level measurements reveal nose-shaped wind profiles with maximum values occurring at about 20-60 m AGL. The frequency of occurrence of persistent down-valley nocturnal jets with a well- defined nose-shape profile in the 0-80 m layer shows little seasonal preference. Their intensity, however, shows a marked seasonality with stronger flows occurring between May and October. Stronger down-valley jets are associated to a more positive curvature of the temperature profile, probably due

to the effect of turbulent mixing. Standard deviation of wind speed suggests that strong turbulence prevails in the full tower layer, despite gradient Richardson numbers being large at the jet nose and above it.

Turbulent mixing also appears to be responsible for the warmer temperatures observed at the lower altitude sites down the valleys. In fact, the mean altitudinal lapse rate of near-surface temperature matches closely the free-tropospheric lapse rate measured at an aerological station located at the coast. Regressions between these upper-air mesurements and the tower observations show that there exists a moderate control of valley nocturnal flows by large scale factors. The highest correlations found are those between the down-valley flow intensity and the temperature difference between the free troposphere and the valley, providing some support for the down-valley wind mechanism. Nevertheless, estimates of terms in the momentum budget for the development and the quasi-stationary phases of the down-valley flows suggest that the pressure gradient force due to the near-surface cooling along the sloping valley axes also plays an important role in these drainage flows. A scale for the height of the wind speed maximun in equilibrium turbulent down-slope jets is proposed based on the surface friction velocity and the surface inversion intensity. At site CAN this scale explains about 70% of the case-to-case variance of the observed jet nose height, although a significant overestimation is found, probably due to an overestimation of the friction velocity.

The flow system reported here has immediate importance in the characterization of the wind energy potential of the Atacama Desert. As mentioned in the Introduction, these measurements were undertaken by the Chilean government in order to explore the possibility of wind farm development in the Atacama region, where the current demand for energy is particularly high. Our results show that, while there is possibly a good wind resource at all measurement sites, the shape and the relationship with stability of the vertical profiles of wind speed sustained by these flows can be quite different to what is commonly found in wind farm sites over flat terrain (e.g. van den Berg 2008), a fact that must be properly taken into

account in the evaluation and design of future wind energy projects in this area. Beyond this applied aspect, further studies should better define the spatial structure and organization of the nocturnal circulation, in order to assess how representative these measurements are of the general low-level wind-regime of the Atacama Desert. Additional investigations should better characterize the evening and morning transitions of these winds and their turbulent structure, as well as elucidate their possible interaction with the coastal boundary layer and subsidence inversion existing to the west and quantify their potential role in the zonal transport of natural and anthropogenic aerosols from the continent to the SEP stratocumulus layer existing offshore. Studies on the numerical modeling and the synoptic forcing of these flows are currently underway in order to address some of these issues.

Acknowledgments.

This research was funded by a cooperation agreement between the University of Chile and the Chilean Ministry of Energy under Exempt Decree 249 of 2013. The measurement campaign in northern Chile was carried out by programs of the Chilean Ministry of Energy, with partial support from the German GIZ Agency (Deutsche Gesellshaft für Internationale Zusammenarbeit GmbH). Special thanks are given to Mr. Christian Santana, then at the Ministry of Energy, for his energy put in initiating these measurement programs.

REFERENCES

André, J. C. and L. Mahrt, 1982: The nocturnal surface inversion and influence of clear-air radiative cooling. *J. Atmos. Sci.*, **39**, 864–878.

Bromwich, D. H., 1989: An extraordinary katabatic wind regime at Terra Nova bay, Antarctica. *Mon. Wea. Rev.*, **117**, 688–695.

Chand, D., D. A. Hegg, R. Wood, G. Shaw, D. Wallace, and D. Covert, 2010: Source attribution of climatically important aerosol properties measured at Paposo (Chile) during VOCALS. *Atmos. Chem. Phys.*, **10**, 10 789–10 802.

Conangla, L. and J. Cuxart, 2006: On the turbulence in the upper part of the low-level jet: an experimental and numerical study. *Boun.-Layer Meteor.*, **118**, 379–400.

Cuxart, J. and M. A. Jiménez, 2007: Mixing processes in a nocturnal low-level jet: an LES study. *J. Atmos. Sci.*, **64**, 1666–1679.

Edwards, J. M., R. J. Beare, and A. J. Lapworth, 2006: Simulation of the observed evening transition and nocturnal boundary layers: Single-column modelling. *Quart. J. Roy. Meteor. Soc.*, **132**, 61–80.

Garreaud, R. and P. Aceituno, 2007: Atmospheric circulation and climatic variability. *The Physical Geography of South America*, A. Orme, T. T. Veblen, and K. Young, Eds., Oxford, 45–59.

Garreaud, R., A. Molina, and M. Farías, 2010: Andean uplift and Atacama hyperaridity: A climate modeling perspective. *Earth Planet. Let.*, **292**, 39–50.

Garreaud, R., 2010: The Andes climate and weather. *Adv. Geosci.*, **7**, 1–9.

505 Mahrt, L., 1982: Momentum balance of gravity flows. *J. Atmos. Sci.*, **39**, 2701–2711.

506 Muñoz, R., R. Zamora, and J. Rutllant, 2011: The coastal boundary layer at the east-
507 ern margin of the South East Pacific (23.4 S, 70.4 W): cloud-conditioned climatology. *J.*
508 *Climate*, **24**, 1013–1033.

509 Parish, T. and D. Bromwich, 1987: The surface windfield over the Antarctic ice sheets.
510 *Nature*, **328**, 51–54.

511 Parish, T., 1982: Surface airflow over East Antarctica. *Mon. Wea. Rev.*, **110**, 84–90.

512 Rutllant, J., H. Fuenzalida, and P. Aceituno, 2003: Climate dynamics along the arid northern
513 coast of Chile: the 1997-1998 Dinamica del Clima de la Región de Antofagasta (DICLIMA)
514 experiment. *J. Geophys. Res.*, **108**, doi:10.1029/2002JD003357.

515 Rutllant, J. and P. Ulriksen, 1979: Boundary-layer dynamics of the extremely arid northern
516 part of Chile. *Boun.-Layer Meteor.*, **17**, 41–55.

517 Savage, L. C., S. Zhong, W. Yao, W. J. O. Brown, T. W. Horst, and C. D. Whiteman,
518 2008: An observational and numerical study of a regional-scale downslope flow in northern
519 Arizona. *J. Geophys. Res.*, **113**, D14114, doi:10.1029/2007JD009623.

520 Schmidli, J., et al., 2011: Intercomparison of mesoscale model simulations of the daytime
521 valley wind system. *Mon. Wea. Rev.*, **139**, 1389–1409.

522 Schmidt, D., 1999: *Das Extremklima der nordchilenischen Hochatacama unter besonderer*
523 *Berücksichtigung der Höhengradienten*, Dresdener Geographische Beiträge, Vol. 4. Tech-
524 nische Universität Dresden, 122 pp.

525 van den Berg, G. P., 2008: Wind turbine power and sound in relation to atmospheric stability.
526 *Wind Energy*, **11**, doi:10.1002/we.240.

527 Wendler, G., C. Stearns, G. Weidner, G. Dargaud, and T. Parish, 1997: On the extraordinary
528 katabatic winds of Adelie Land. *J. Geophys. Res.*, **102**, doi:10.1029/96JD03438.

Whiteman, C. D. and J. C. Doran, 1993: The relationship between overlying synoptic-scale flows and winds within a valley. *J. Appl. Meteor.*, **32**, 1669–1682.

Whiteman, C. D. and S. Zhong, 2008: Downslope flows on a low-angle slope and their interactions with valley inversions. Part I: Observations. *J. Appl. Meteor. Climatol.*, **47**, 2023–2038.

Whiteman, C. D., 1990: Observations of thermally developed wind systems in mountainous terrain. *Atmospheric processes over complex terrain*, W. Blumen, Ed., American Meteorological Society, 5–42.

Whiteman, C. D., 2000: *Mountain Meteorology: Fundamentals and Applications*. 1st ed., Oxford, 355 pp.

Wolter, K. and M. S. Timlin, 2011: El Nino/Southern Oscillation behaviour since 1871 as diagnosed in an extended multivariate ENSO index (MEI.ext). *Int. J. Climatol.*, **31**, 1074–1087.

List of Tables

TABLE 1. Measurement heights and main NRG Systems Inc. sensors available in 80 m towers.

variable	heights (m AGL)	sensors	main characteristics
wind speed	10, 20, 40, 60, 80	NRG#40C	3-cup anemometer; 0.78 m s^{-1} threshold; 3.0 m distance constant.
wind direction	10, 40, 80	NRG#200P	continuous rotation potentiometer; 1.0 m s^{-1} threshold.
temperature	2, 40, 80	NRG#110S	integrated circuit temperature sensor; 10 min thermal time constant.

TABLE 2. Correlation coefficients between tower measurements and Antofagasta radiosonde data in the 2000 - 3000 m ASL layer (May-October).

tower variable	Antofagasta-related variable	CAN	CAO	SGE
DVWS40	ESE-SE Wind	0.41	0.53	0.49
DVWS40	TANTO	0.54	0.54	0.62
DVWS40	TANTO-TZNIGHT	0.60	0.71	0.81

List of Figures

12 a) May-October average of down-valley projected wind speed at 40 m AGL (continuous) for stations CAN (blue), CAO (green) and SGE (red) for period between 16 and 08 LT. b) As a), but for 40 m - 02 m temperature difference (continuous), 80 m - 40 m temperature difference (dashed), and mean surface solar radiation scaled by 150 (shaded). c) Scatter plot between observed jet nose heights (ZX) and estimates based on equation (6) for station CAN. d) as c) but for CAO. e) as c) but for SGE. In order to have a continuous estimate of ZX, a second-order polynomial was fitted to the three data levels around the observed wind speed maximum. 41

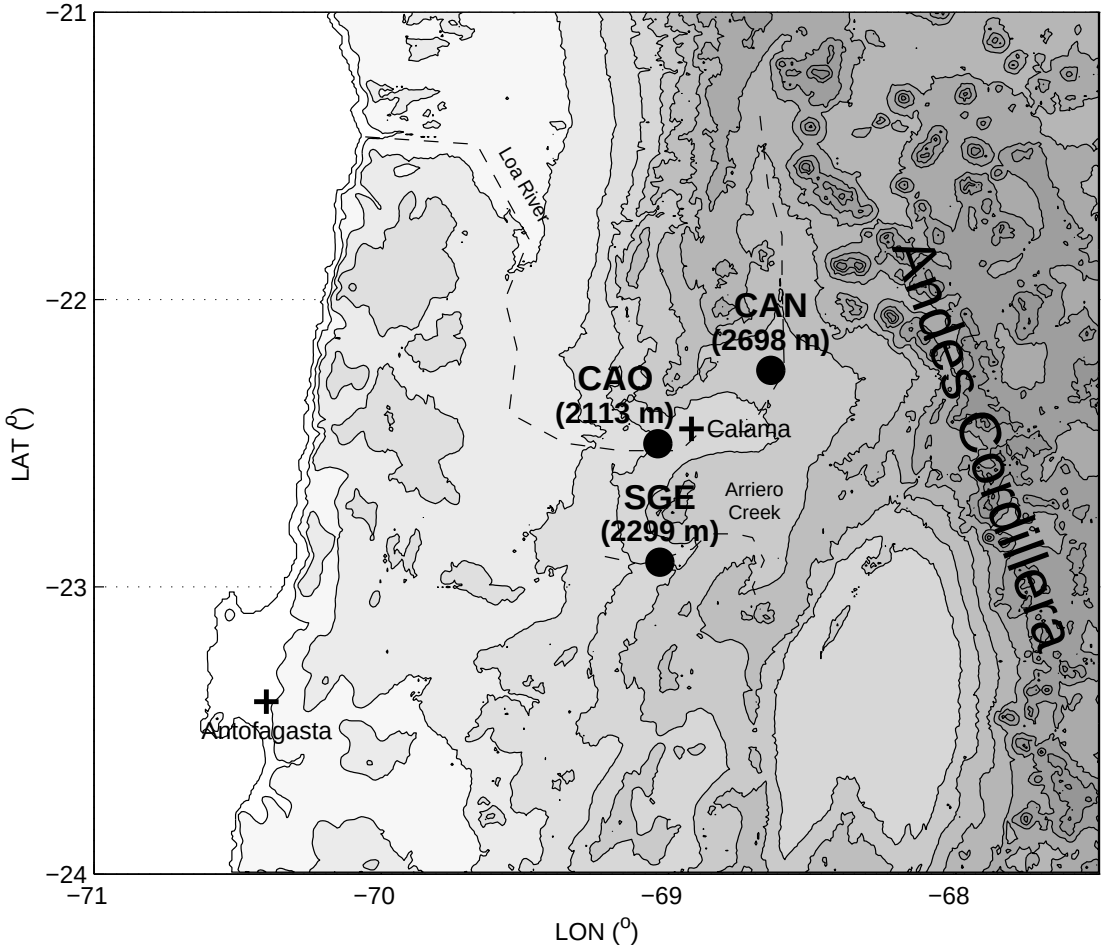

FIG. 1. Topography of the study region and location of 80-m towers (altitude of the stations shown in parenthesis). Terrain heights are contoured from 0 to 6000 m ASL every 500 m. Pluses (+) indicate radiosonde station (Antofagasta) and Calama city. Dashed lines mark Loa River and Arriero Creek.

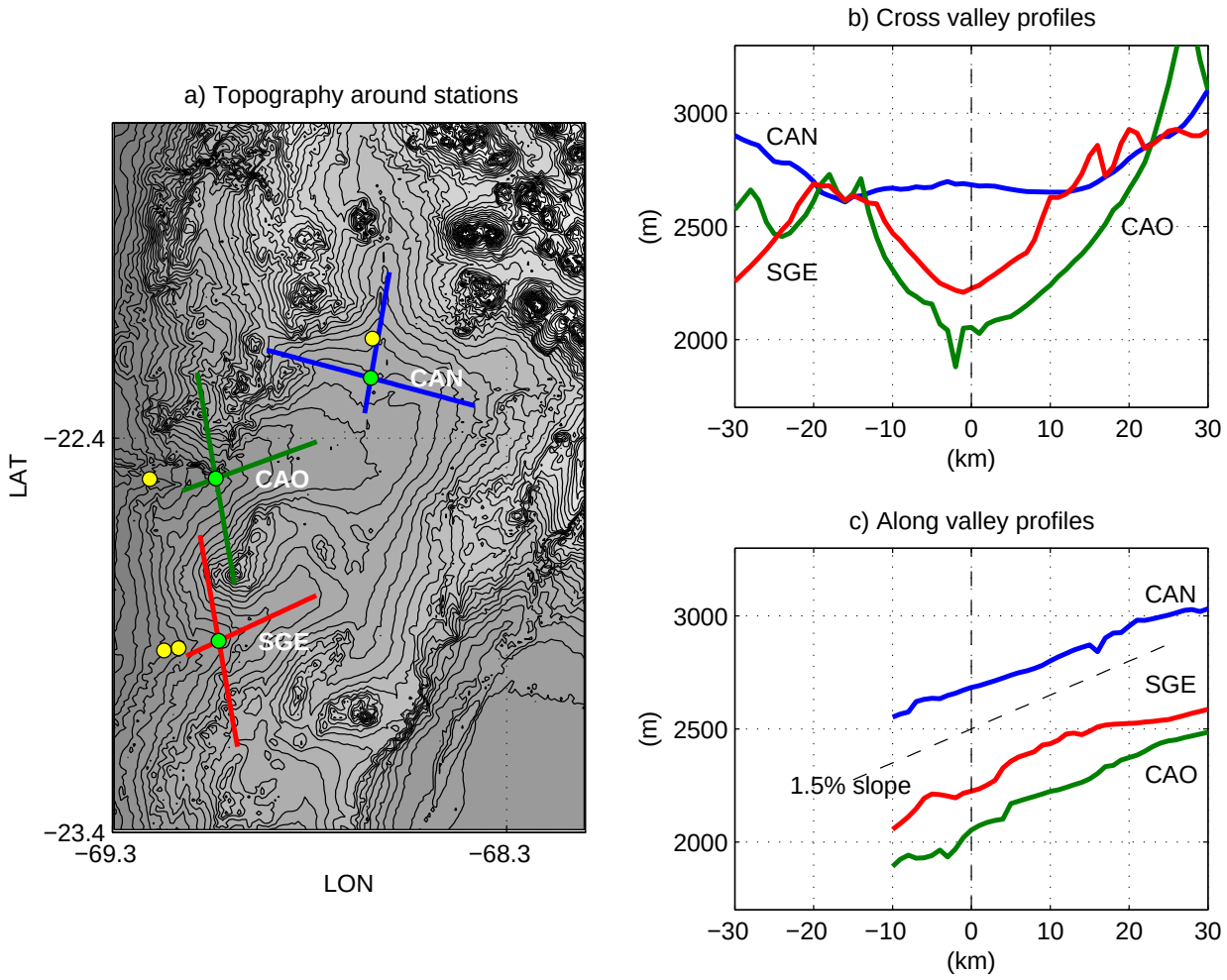

FIG. 2. a) Topography around 80-m towers. Lines indicate location of sections shown in b) and c). Contours drawn every 100 m. Yellow circles indicate locations of 20-m meteorological masts referred to in Fig. 11. b) Cross-valley topographic profiles around each station. The zero in the abscissa marks the position of the tower. c) as b), but for along-valley topographic profiles. In all panels, stations CAN, CAO and SGE are denoted by colors blue, green and red, respectively.

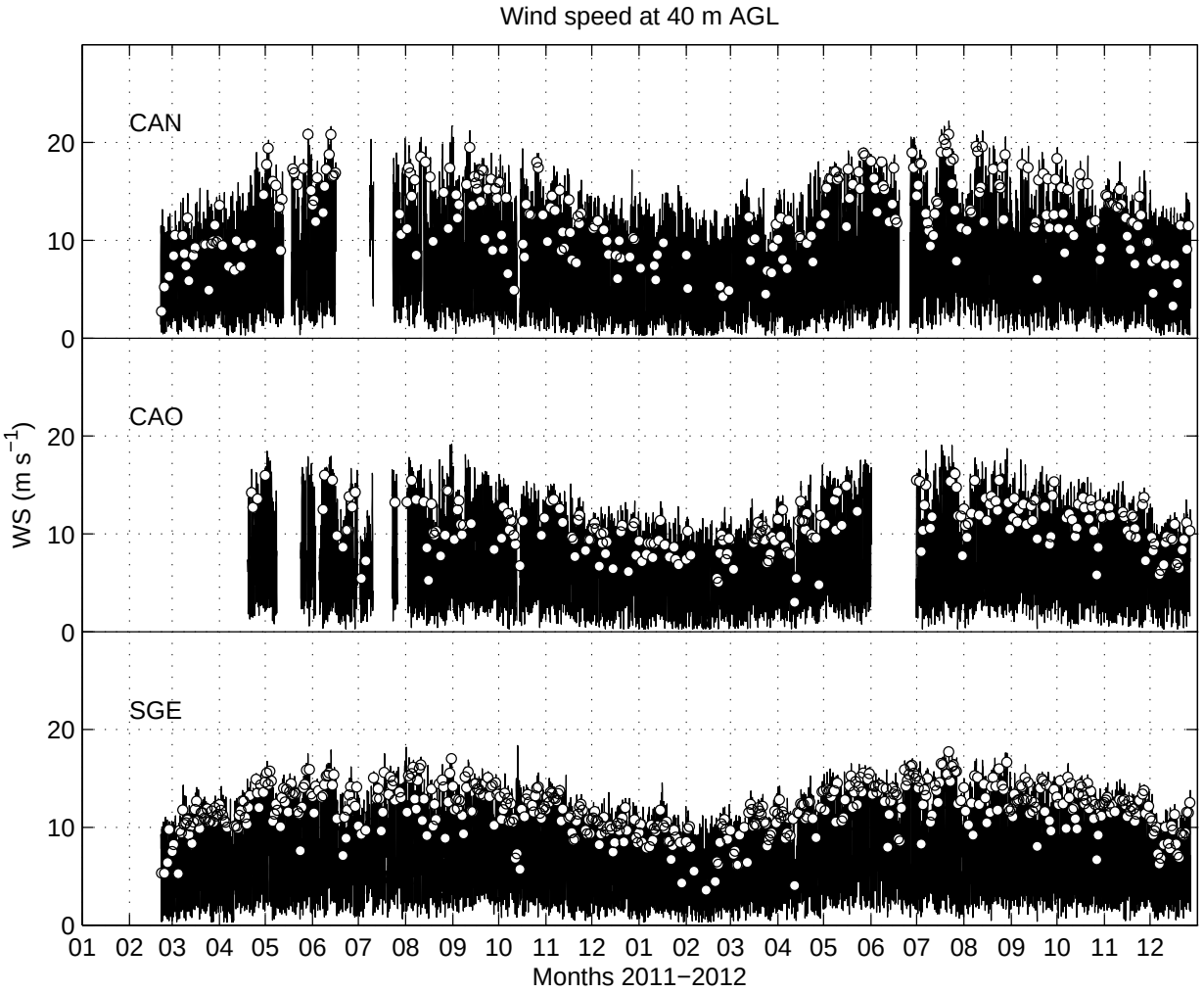

FIG. 3. Continuous lines show the complete time series of hourly averaged wind speed measured at 40 m AGL at stations CAN (upper), CAO (middle) and SGE (bottom). White circles correspond to 02-06 LT averages for down-valley jet cases (see text). Measurements at all stations started on February 2011, although at CAO wind measurements at 40 m and above were operational only from April 2011 onwards.

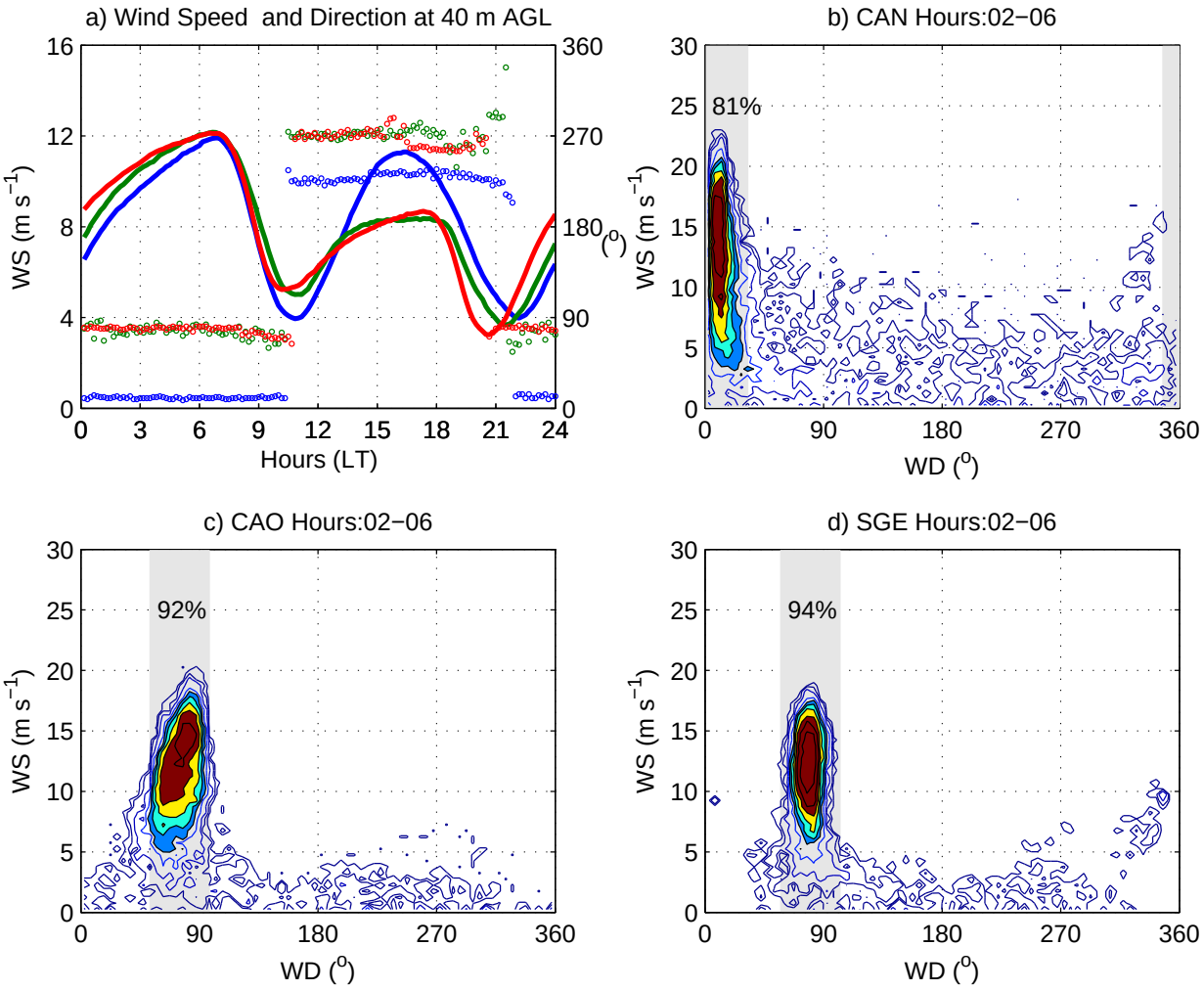

FIG. 4. a) Diurnal cycles of mean wind speed (lines, left scale) and most frequent wind direction (circles, right scale) measured at 40 m AGL for the full period of record at CAN (blue), CAO (green) and SGE (red). b) CAN wind direction-wind speed joint frequency distribution at 40 m AGL for 10-minute averages in the 02-06 LT period. Frequency contours are logarithmically spaced in order to display infrequent occurrences (line contours) and more common occurrences (colored contours). c) as b) but for CAO. d) as b) but for SGE. Gray-shaded regions in b)-d) mark the down-valley direction sectors defined for each station. The percentage of 02-06 LT wind direction observations falling in this sector is annotated for each site.

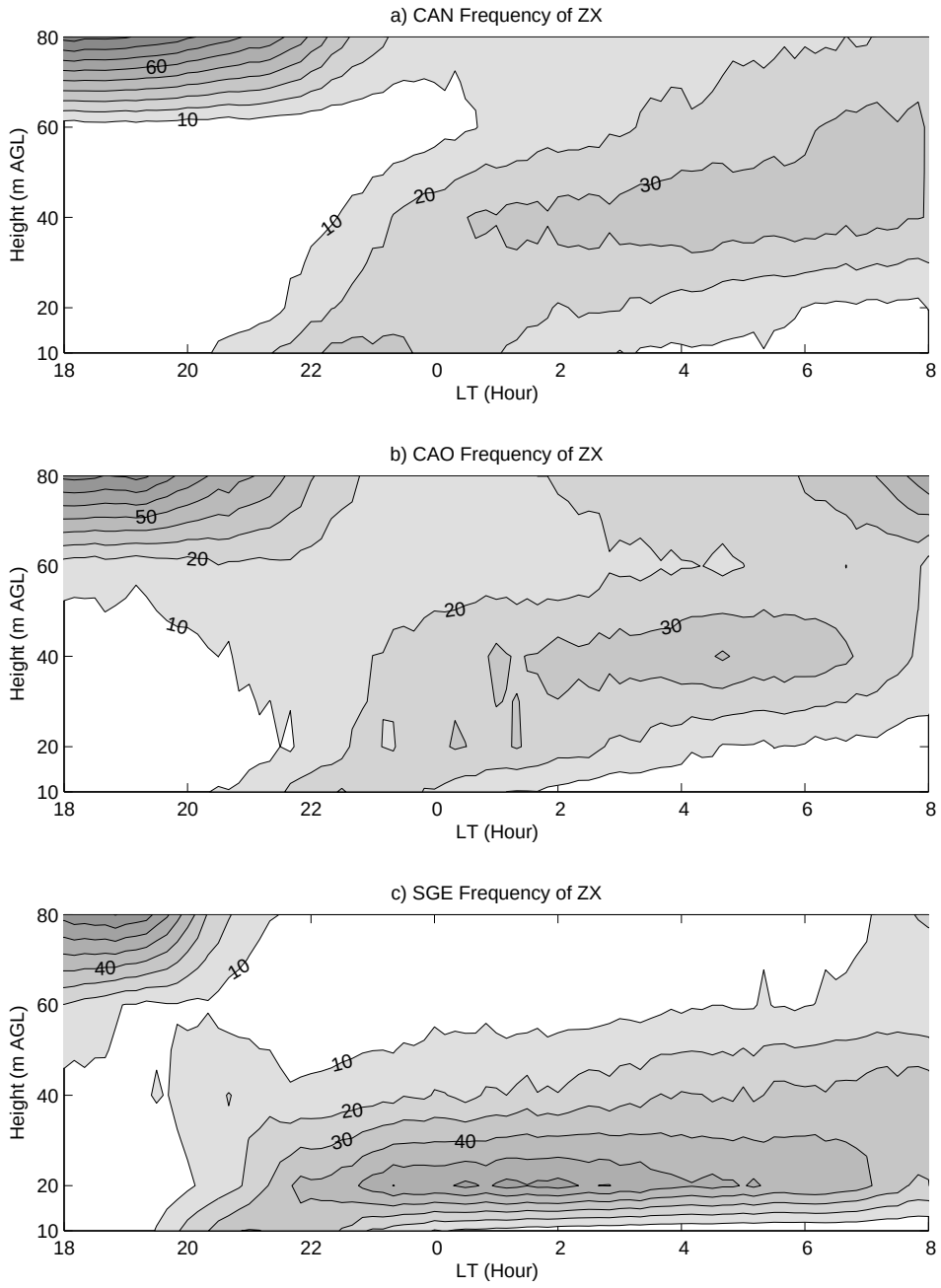

FIG. 5. Time evolution of the frequency distribution of the height of maximum wind speed (ZX) measured at a) CAN, b) CAO, c) SGE. Frequency contours drawn from 10% to 90% every 10%. Only the period from 18 to 08 LT is shown with 10-minute time resolution. Wind speed data is available only at measuring heights of 10 m, 20 m, 40 m, 60 m, and 80 m AGL. The full period of record at each station has been considered.

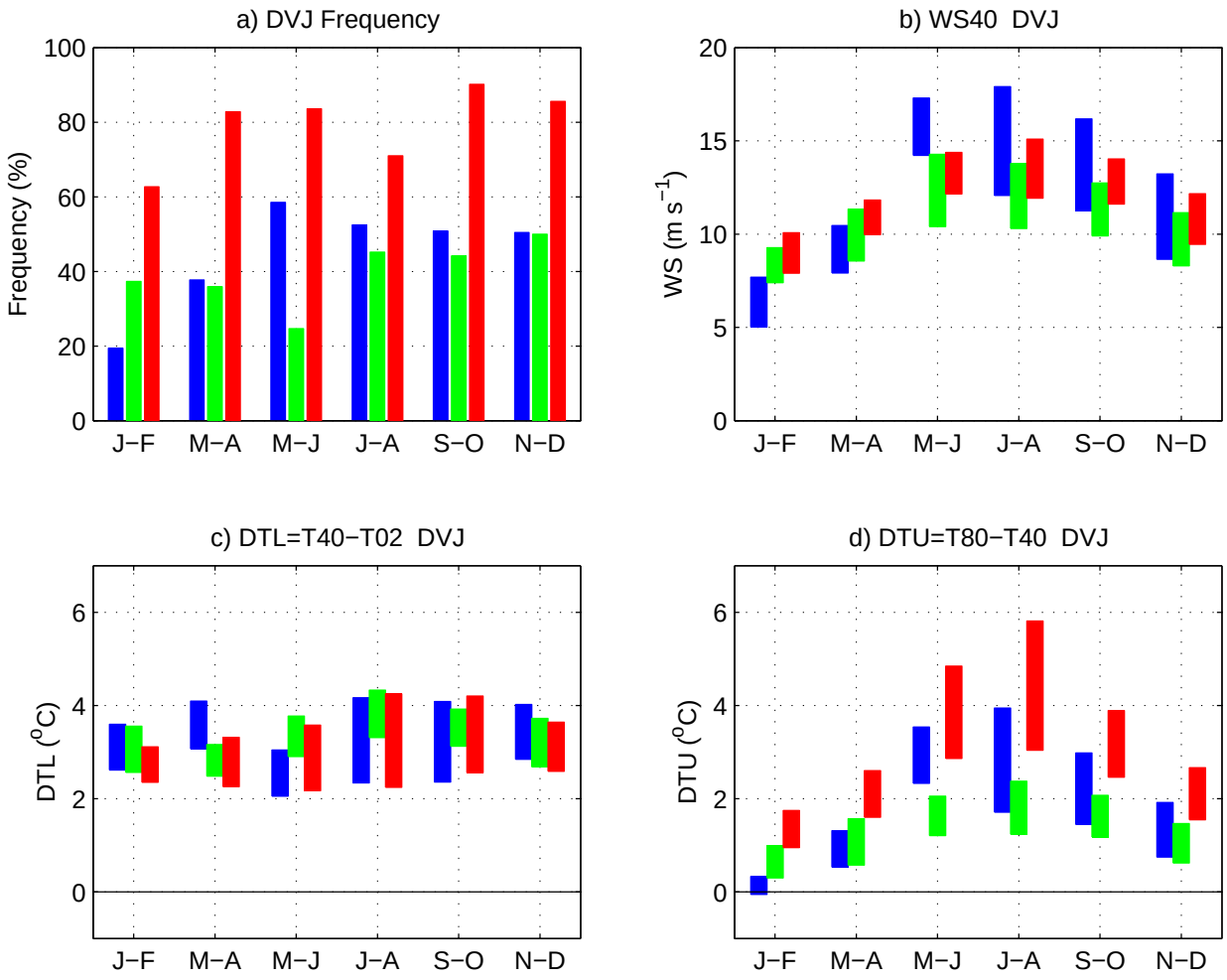

FIG. 6. a) Bi-monthly occurrence frequency of down-valley jets (DVJs) as defined in the text. b) Bi-monthly variation of inter-quartile ranges of DVJ intensities at 40 m AGL averaged in the 02-06 LT period. c) As b) but for 40 m-02 m temperature difference during DVJ events. d) As c) but for 80 m-40 m temperature difference. In all panels colors blue, green and red refer to stations CAN, CAO and SGE, respectively.

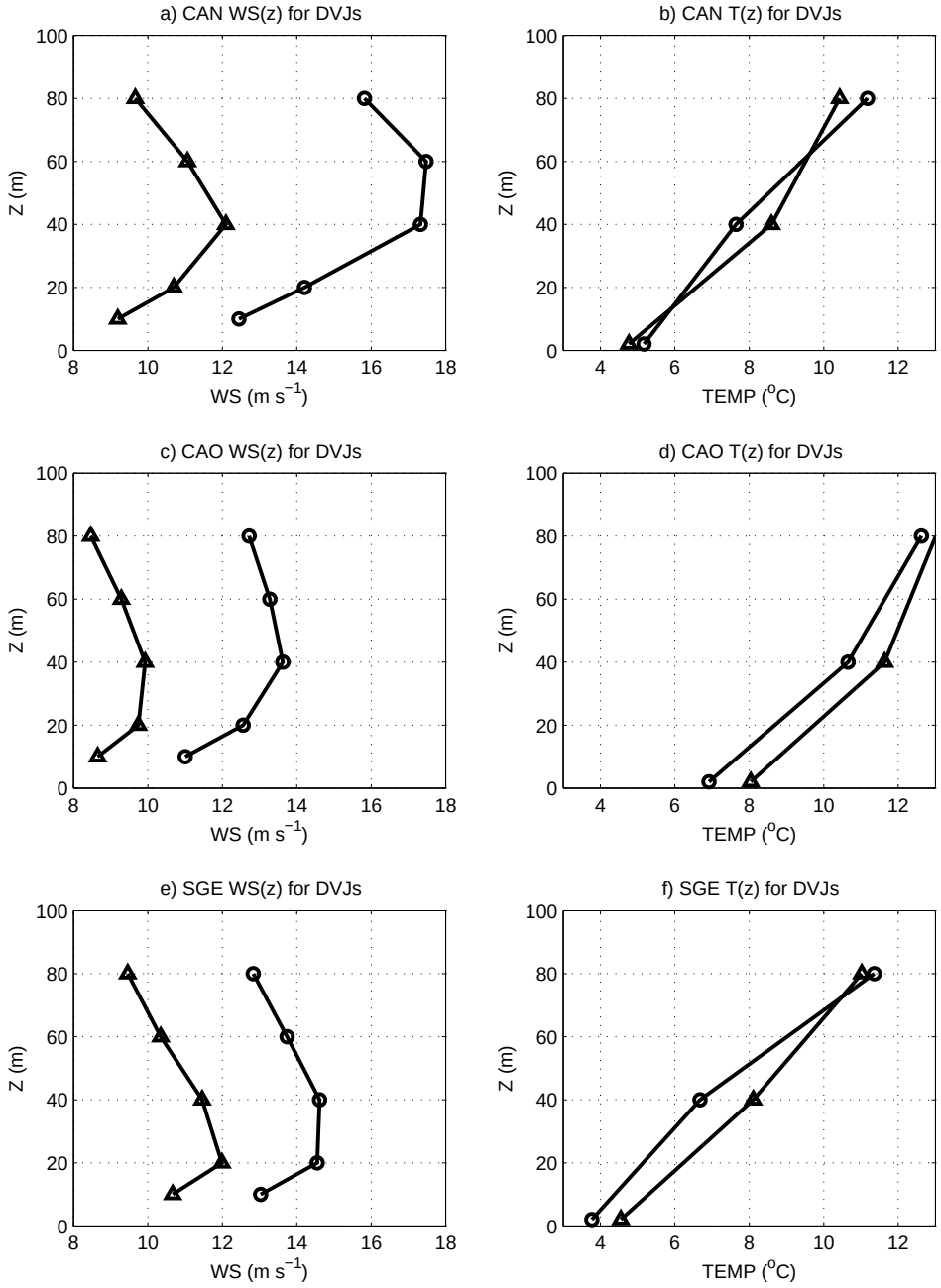

FIG. 7. Vertical profiles of 02-06 LT-averaged wind speed (left panels) and temperature (right panels) averaged over strong (circles) and weak (triangles) DVJs for the months of May to October at stations CAN (upper), CAO (middle) and SGE (bottom). Threshold between weak and strong DVJs is based on the median of WS40 at each site (15.4 m s^{-1}, 11.8 m $^{-1}$, and 13.3 m $^{-1}$ for CAN, CAO, and SGE, respectively).

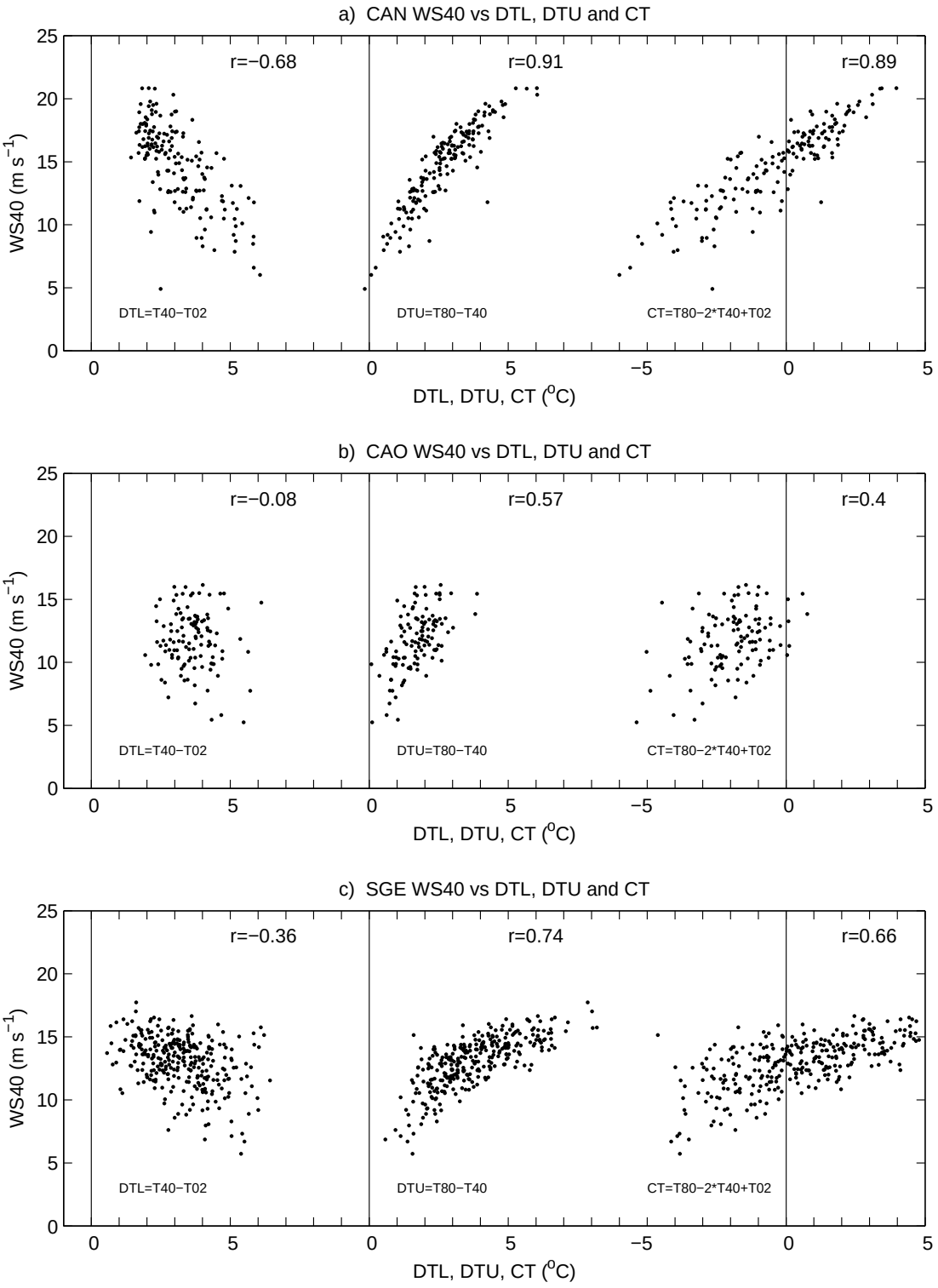

FIG. 8. a) Dispersion between WS40 and DTL (left), DTU (center), and CT (right) for DVJ cases in the months from May to October at the CAN site. b) As a) but for CAO. c) As a) but for SGE. See text for definition of indices.

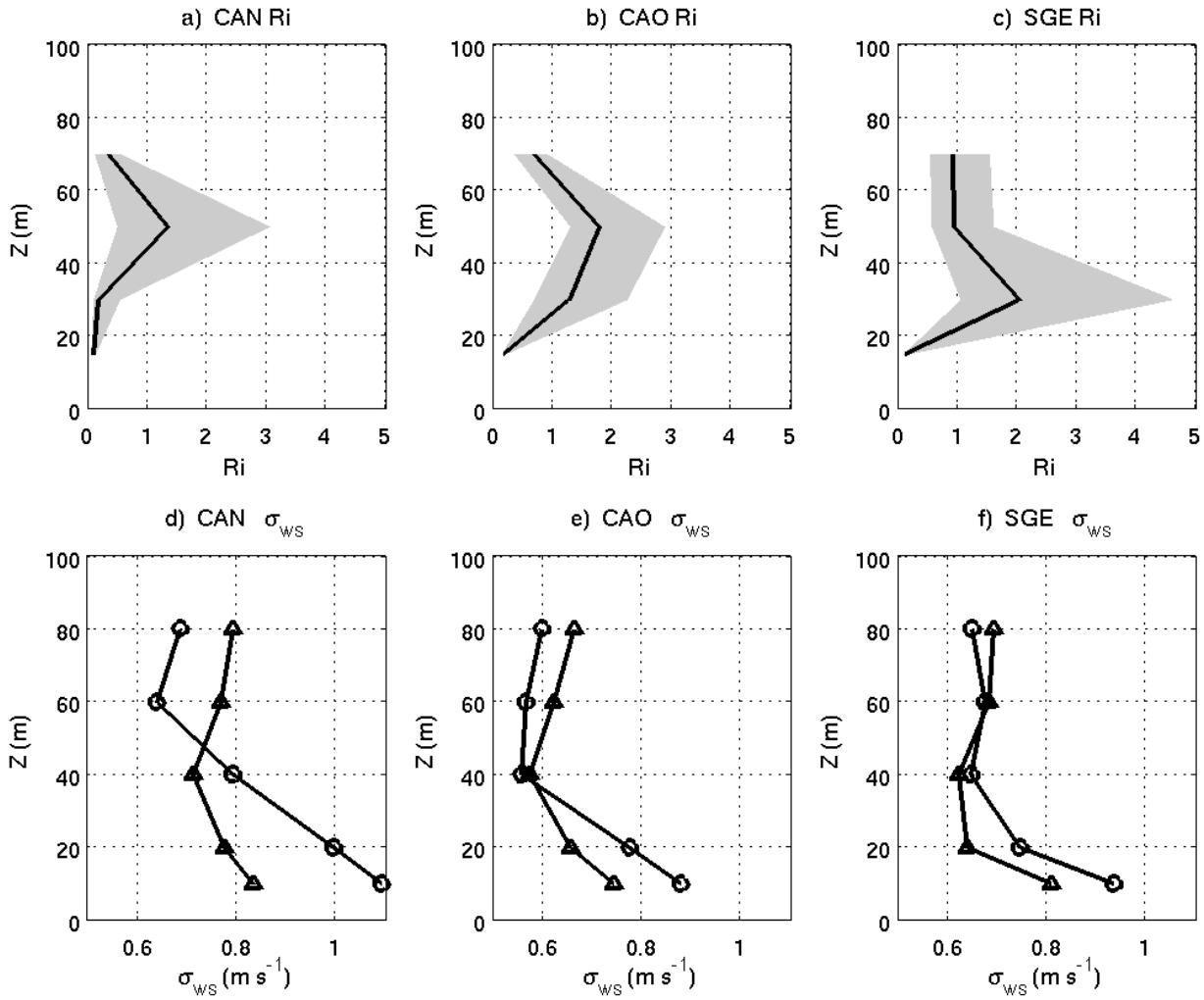

FIG. 9. Upper panels: Vertical profiles of Richardson numbers during DVJ events (02-06 LT averages). Shading marks the inter-quartile range and continuous line marks the median values. Lower panels: Vertical profiles of wind speed standard deviation averaged over strong (circles) and weak (triangles) DVJs. Left, middle and right panels correspond to stations CAN, CAO and SGE, respectively. Analysis period includes the months from May to October.

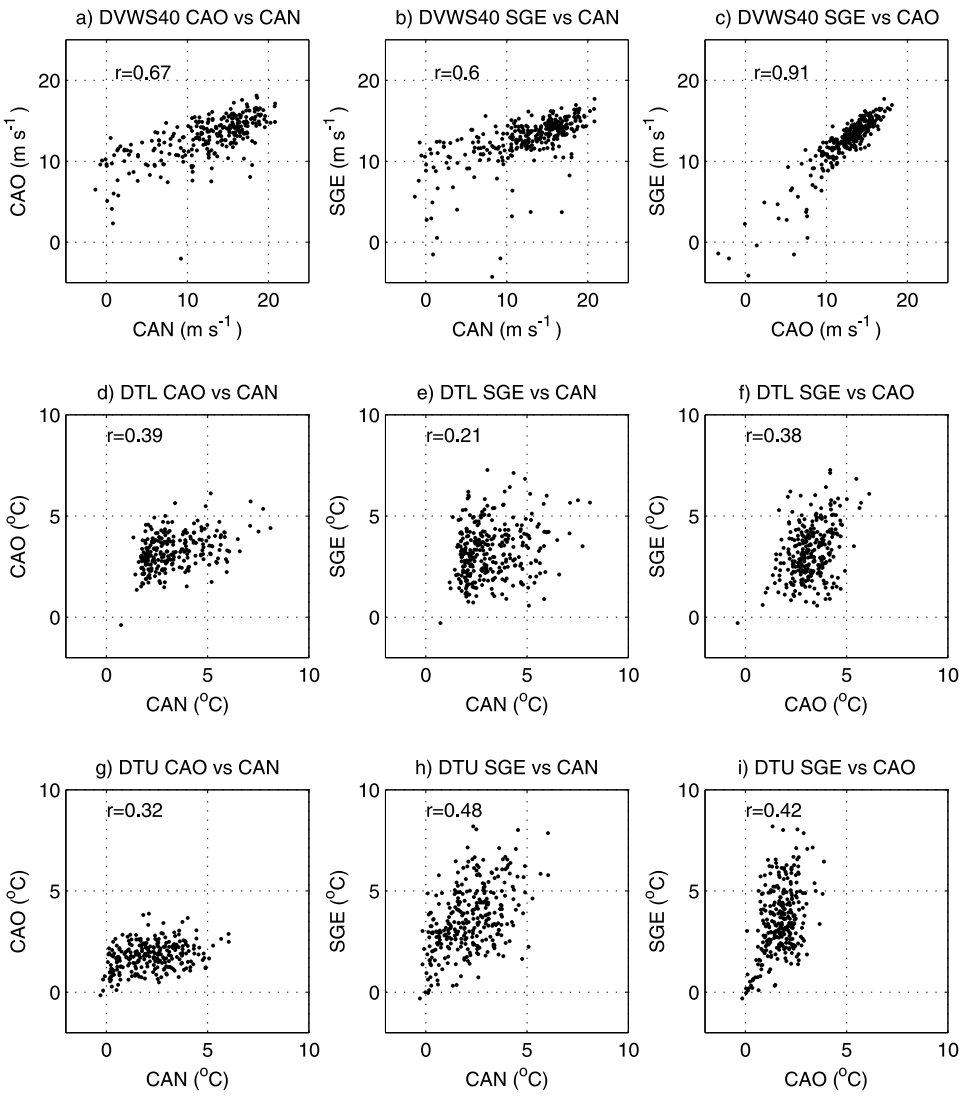

FIG. 10. Upper panels: co-variability of DVWS40 among the stations. Middle panels: co-variability of DTL among the stations. Lower panels: co-variability of DTU among the stations. Analysis period includes the months from May to October.

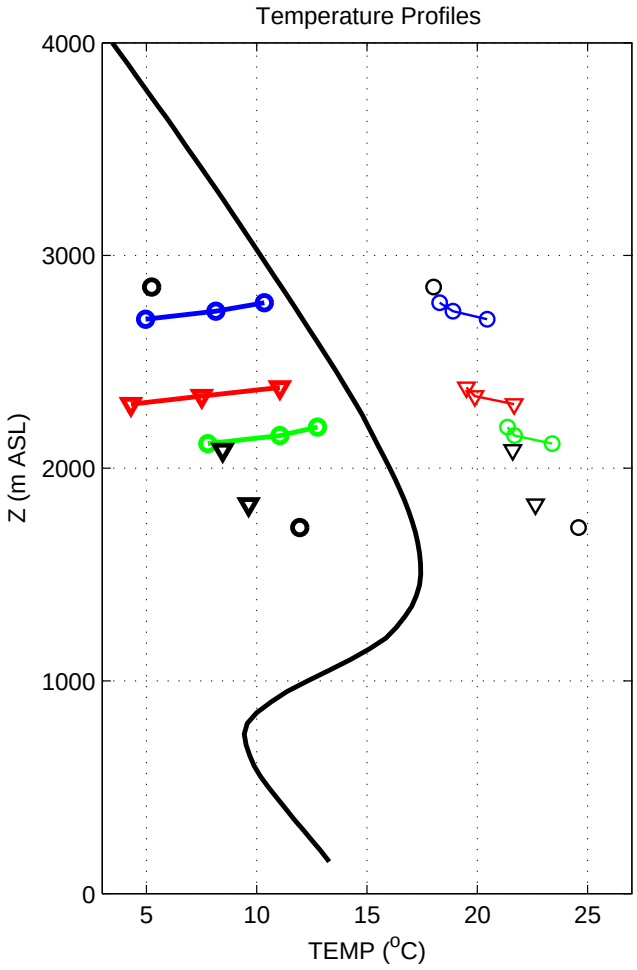

FIG. 11. Temperatures averaged over the months from May to October plotted agains the altitude above sea level of the sensor. Black continuous line: 12 UTC (08 LT) Antofagasta radiosondes. Colored profiles for 02-06 LT (bold) and 14-18 LT (fine) averages at CAN (blue), CAO (green) and SGE (red). Black symbols: 02-06 LT (bold) and 14-18 LT (fine) averages of 5-m temperatures measured at 20-m meteorological masts (locations shown in Fig. 2). Triangles and circles indicate stations located along Arriero Creek and Loa River valleys, respectively.

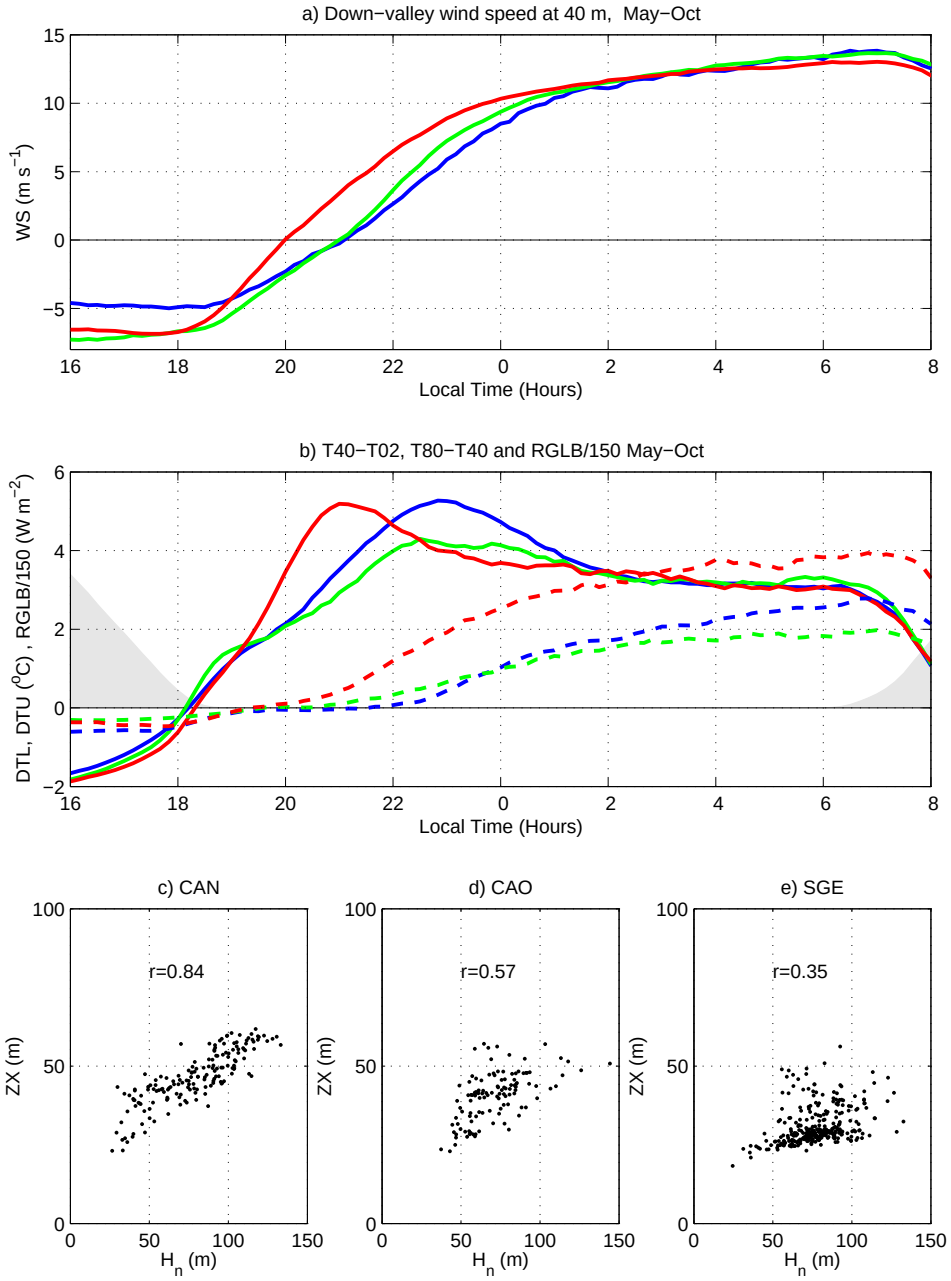

FIG. 12. a) May-October average of down-valley projected wind speed at 40 m AGL (continuous) for stations CAN (blue), CAO (green) and SGE (red) for period between 16 and 08 LT. b) As a), but for 40 m - 02 m temperature difference (continuous), 80 m - 40 m temperature difference (dashed), and mean surface solar radiation scaled by 150 (shaded). c) Scatter plot between observed jet nose heights (ZX) and estimates based on equation (6) for station CAN. d) as c) but for CAO. e) as c) but for SGE. In order to have a continuous estimate of ZX, a second-order polynomial was fitted to the three data levels around the observed wind speed maximum.